Scalable fabrication of efficient p-n junction lead sulfide quantum dot solar cells

Author(s):
Goossens, Vincent M.; Sukharevska, Nataliia V.; Dirin, Dmitry N.; Kovalenko, Maksym V.; Loi, Maria A.

Publication date:
2021-12-22

Permanent link:
https://doi.org/10.3929/ethz-b-000522565

Originally published in:
Cell Reports 2(12), https://doi.org/10.1016/j.xcrp.2021.100655

Cell Reports
Physical Science

CellPress
OPEN ACCESS

Article

Scalable fabrication of efficient p-n junction lead sulfide quantum dot solar cells

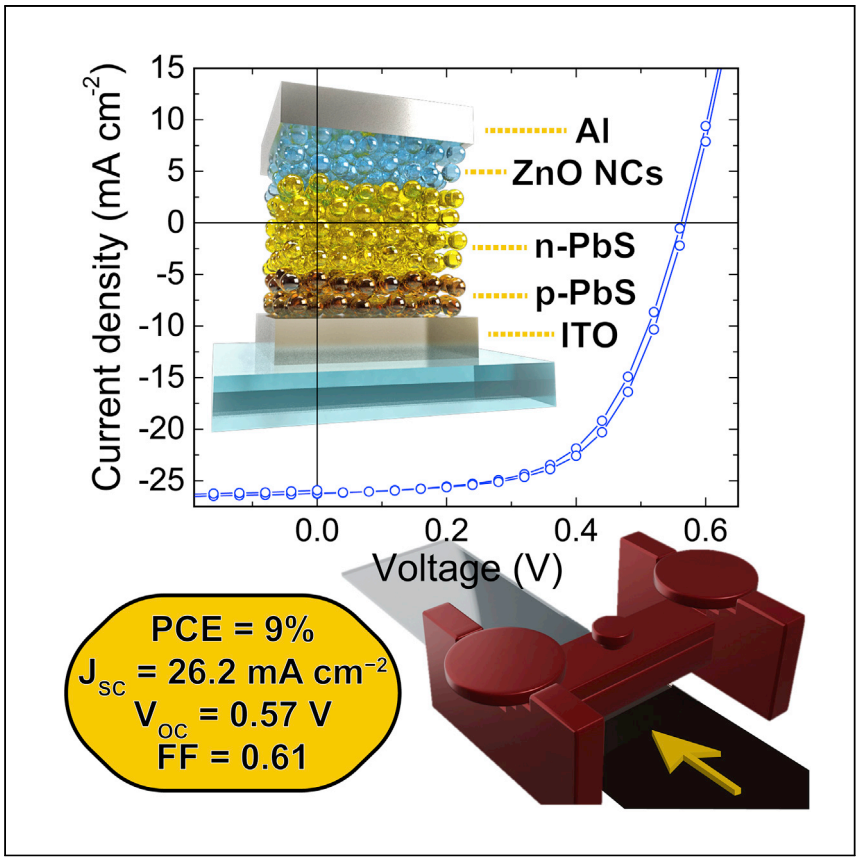

PbS colloidal quantum dot solar cells with p-n structure are yet to be fabricated by scalable methods. Goossens et al. propose a scalable fabrication strategy for efficient PbS colloidal quantum dot solar cells with p-n structure, and an industrially suitable technique is used without compromising performance.

Vincent M. Goossens, Nataliia V. Sukharevska, Dmitry N. Dirin, Maksym V. Kovalenko, Maria A. Loi

m.a.loi@rug.nl

Highlights

Scalable fabrication of p-n structure PbS CQD solar cells

Blade coating optimized for both p- and n-type PbS CQD layers

Blade-coated PbS CQD solar cells with p-n architecture accomplish a PCE of 9.0%

This PCE is close to the record for p-n structures fabricated by spin coating

Goossens et al., Cell Reports Physical Science 2, 100655
December 22, 2021
https://doi.org/10.1016/j.xcrp.2021.100655

Cell Reports
Physical Science

CellPress
OPEN ACCESS

Article

Scalable fabrication of efficient p-n junction lead sulfide quantum dot solar cells

Vincent M. Goossens,[1,4] Nataliia V. Sukharevska,[1,4] Dmitry N. Dirin,[2,3] Maksym V. Kovalenko,[2,3] and Maria A. Loi[1,5,*]

SUMMARY

Nowadays, the best lead sulfide (PbS) colloidal quantum dot (CQD) solar cells are primarily demonstrated in the n-p structure, while the p-n structure is significantly less developed. This technological gap between the n-p and p-n structures is much more distinct than in cases of other solution-processable photovoltaic technologies like perovskites and polymers. Here, we propose a scalable fabrication strategy for efficient PbS QD solar cells with p-n structure. An industrially suited blade-coating technique has been used to deposit both n-type and p-type QD layers. The obtained solar cells demonstrated power conversion efficiency of 9%, thus, commensurate to the record device efficiency with this architecture fabricated with a non-scalable technique. The availability of both p-n and n-p structures fabricated from scalable methods may promote the future integration of the PbS QDs into tandem devices together with other solution-processable materials to exploit the most prominent benefits of the PbS QDs, such as infrared absorption.

INTRODUCTION

Lead sulfide (PbS) colloidal quantum dots (CQDs) show great promise for optoelectronics due to the combination of well-developed and partially scalable synthesis, facile control of the surface chemistry, solution-based processing, and band-gap tunability by size.[1] In a similar manner to the bulk semiconductors, PbS CQD solids benefit from controlling the charge carrier's concentration and mobility by doping, as it allows building p-n junctions, which are at the core of efficient optoelectronic devices. However, achieving doping in CQDs greatly differs from bulk materials and most of the time is accomplished by employing various surface modifications.[2,3] This strategy has significantly advanced in the last few years the design and development of PbS CQDs field-effect transistors (FETs),[4,5] light-emitting diodes (LEDs),[6] light-emitting FETs (LEFETs),[7,8] photodetectors,[9] and inverters.[10]

PbS CQD-based solar cell devices benefit particularly from low-cost scalable production of large-area thin film and spectral tunability.[11–17] PbS has an energy band gap of 0.4 eV in bulk single crystals and a large exciton Bohr radius of 18 nm. As a result, PbS CQDs can be tuned in size to control which part of the near-infrared (IR) region of the solar spectrum is harvested.[18,19] This feature is highly desirable for the construction of tandem solar cells.[19–24] Furthermore, the capacity to exploit multiple exciton generation and the potential for hot charge carrier extraction, together with the mentioned IR spectral tuning, could offer the opportunity to overcome the Shockley-Queisser efficiency limit.[16,17]

[1]Zernike Institute for Advanced Materials, Nijenborgh 4, Groningen 9747 AG, the Netherlands

[2]Department of Chemistry and Applied Biosciences, ETH Zurich, Vladimir Prelog Weg 1, Zurich 8093, Switzerland

[3]Empa-Swiss Federal Laboratories for Materials Science and Technology, Uberlandstr. 129, Dubendorf 8600, Switzerland

[4]These authors contributed equally

[5]Lead contact

*Correspondence: m.a.loi@rug.nl

https://doi.org/10.1016/j.xcrp.2021.100655

The record power conversion efficiency (PCE) of PbS CQD solar cells is currently about 14%.[13,25–27] This impressive result has been obtained thanks to a collective effort that has, in the last few years, enabled a large progress in the synthesis of PbS CQDs,[18,28,29] development of the chemical surface modification strategies,[29] ligand exchange for trap passivation,[12,20] and adjustment of electronic properties.[2,30] Furthermore, the colloidal stability of QDs with short ligands has been improved,[31,32] and new efficient deposition methods for CQDs solids have been developed.[9,14,19,33–36]

Nowadays, all of the best PbS CQD solar cells are based on n-p structures,[12,26,27] most of which include a transparent conductive substrate; n-type wide band-gap metal oxide (electron transport layer [ETL]); n-type PbS CQDs (mostly PbS-X, where X are halogen ions); p-type PbS CQDs (mostly PbS-EDT, where EDT is 1,2-Ethanedithiol); sometimes an HTL (hole transport layer); and gold as a back contact. Besides efficiency, the n-p structure also significantly outperformed the devices with p-n structure in other aspects including stability[37–39] against oxidation and internal degradation.[40] The availability of an efficient p-n CQD solar cell could offer more flexibility in the design of future tandem solar cell devices when CQD solar cells are in conjunction with other emerging types of semiconductors. Here, it is important to underline that Pb chalcogenide CQDs have a large importance in the development of solution-processable multijunction thin film solar cells, as they are the only solution-processable material able to harvest near-IR light.[19–21] However, there are only a few relatively recent reports on p-n CQD solar cells with acceptable performances.[41–43]

To become commercially relevant, scalable fabrication is as essential as the device's PCE for any photovoltaic technology. The CQD community realized that one of the most crucial tasks in building a CQD-based solar cell technology is the scalability of the fabrication processes, and recently, more effort has been put into the scalable fabrication of CQD solar cells. The largest challenges on the way toward scalable p-n PbS CQDs solar technology are: (1) production of the p-type inks,[14,27] in order to completely discard the material wasteful and not scalable layer-by-layer (LbL) casting;[44–46] (2) colloidal stability of both p-type and n-type PbS CQD inks;[12,31,33,47] (3) the orthogonality of the processing solvents used for casting subsequent layers;[21] and (4) the adaptation of the laboratory-scale deposition to the real manufacturing techniques.[9,14,19,33–36]

In this work, we present a scalable approach to fabricate highly efficient p-n structure CQD solar cells by sequential blade casting of PbS CQDs capped by 3-Mercaptopropionic acid (MPA; p-type inks) and by lead halides (n-type inks). The layer casting and the solution-based ligand exchanges were accomplished under ambient conditions, which greatly simplified fabrication and allowed for high throughput. Our multilayer solution casting strategy became possible due to the optimization of the p-type inks with sufficient colloidal stability, optimization of the substrate wettability, and the ability to employ orthogonal solvents. As a result, our fully blade-coated CQD solar cells with p-n architecture accomplished a PCE of 9.0%. This is very close to the current 9.7% record for p-n structure fabricated by spin coating.[41] Furthermore, our device outperforms in the open-circuit voltage (V_{OC}) and exhibits some storage stability, as its efficiency remains practically the same upon keeping the devices in ambient conditions for 2 weeks.

RESULTS AND DISCUSSION

Scalable fabrication of PbS QD solar cells in p-n structure

One of the challenges for scalable fabrication of PbS CQD solar cells is the p-type CQD layer's deposition. In fact, the p-type layer in this type of solar cells is usually

composed of PbS CQDs capped by EDT ligands (PbS-EDT). For the deposition of this layer, *in situ* multistep solid-state ligand exchange is required. On the contrary, for the n-type CQD layer, ligand-exchanged inks, suited for a single-step deposition, were lately applied. These inks are obtained with the in-solution ligand-exchange, concomitant with the phase-transfer into a more polar solvent.

To make a p-type ink using EDT ligands does not seem possible because of the two thiol functional groups, which rather tend to link nanocrystals (NCs) instead of giving rise to a colloidal dispersion. In fact, the separation of these thiol groups with two methylene groups and the very high reactivity of the thiol groups themselves makes the bidentate binding of the EDT molecule to one or two neighboring NCs extremely probable.[48] Therefore, EDT was widely used for PbS CQD solids to cross-link the CQDs for better electronic coupling.[49] Thus, aggregation of PbS CQDs capped by these ligands in solution phases is unsurprising.

Nevertheless, some examples of surface modification for p-type inks were recently demonstrated, among them ligands such as cysteamine (PbS-Cys),[27] 1-thioglycerol (PbS-TG),[27,50] 3-MPA (PbS-MPA),[14,27] chalcogenitometallates,[51] and some others.[52] PbS CQDs with these ligands could potentially replace the PbS-EDT layer.[46] The majority of these p-type PbS CQD inks use capping ligands containing thiol-anchoring groups as the enrichment of the surface with the sulfur that is necessary for the task.[53] Therefore, to obtain a p-type ink for our PbS solar cells, we decided to use 3-MPA.

PbS-MPA CQD solids were widely investigated in early works, and the electronic properties were shown to be comparable to PbS-EDT;[54,55] some studies denoted that MPA can improve the colloidal stability in butylamine (BA) solutions.[31] In the recent literature, there are several examples of PbS CQD solution ligands exchanged with MPA, including a recent one where PbS-MPA p-type inks were successfully implemented in solar cells (with n-p structure).[14] Therefore, we adapted this last recipe, but we increased the concentration of MPA because the phase transfer and phase separation did not occur using the literature-reported recipe. Our attempts to fabricate the n-p structure were unsuccessful, as the p-type PbS layer's deposition from the H_2O and BA mixture dissolved the underlying n-type layer, PbS-PbX_2, cast from pure BA, so we decided to use the p-n structure.

Therefore, we fabricated device structures composed of a layer of PbS CQDs capped by MPA as a p-type layer deposited directly on an indium tin oxide (ITO) anode then a layer of PbS CQDs treated by a mixture of lead halogen salts (PbS-PbX_2) as an n-type layer, a ZnO NC thin film as an electron transporting (ETL) and hole-blocking layer, and an Al back contact. The device structure is schematically represented in Figure 1A. For both n-type and p-type inks, PbS CQDs capped initially by oleic acid (PbS-OA) with the first excitonic peak in the absorption spectrum at 915 nm were used (see Figure S1 for the absorption and PL [photoluminescence] spectra of the original PbS-OA CQD solutions).

Figure 1B shows the schematic energy band diagram of the different layers used in the device. The layers allow for a graded landscape that promotes charge separation and extraction. The ZnO NCs effectively block holes, but electrons are only partially blocked by the PbS-MPA (vide infra). Eventually a better device structure should include an HTL capable of effectively blocking electrons.

Figures 2A and 2B represent the blade-coating deposition process. The technique involves a moving blade over the substrate. A small tunable gap between the

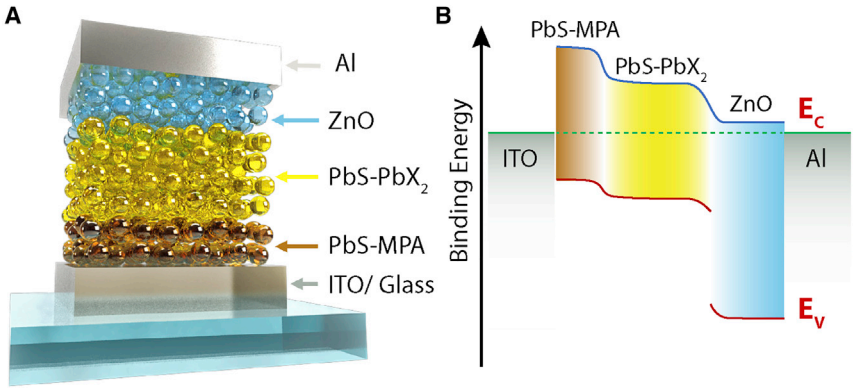

Figure 1. The device structure and energy levels

(A) p-n structure CQD solar cell, whereby the PbS-MPA and PbS-PbX_2 layers are deposited by blade coating. The thickness of the layers is not to scale.

(B) Energy band diagram of our p-n structure solar cell at short-circuit conditions.

substrate and the blade determines the amount of solution that will be spread. Therefore, together with the physical and chemical properties of the solution (concentration, viscosity, density, colloidal stability, reactivity), the properties of the underneath layer (surface energy, roughness), the process temperature, and the speed of the blade are defining the final thickness and morphology of the thin film. Most important, blade coating is a scalable technique and can be adapted for production at the industrial level because of its similarity to roll-to-roll and screen printing. One of the requirements in using blade coating for the deposition of multilayer devices is the processing solvents orthogonality and the bottom layer's resistance to the deposition of the subsequent layer. The exposure of the deposited layers to the following layer's solutions can cause pinholes, cracks, and delamination of the film underneath as well as electronic traps, which can hinder the performance of the working device. This issue is often related to the non-orthogonality of the solvents. However, when the solvents of two adjacent layers are truly orthogonal (and thus of a very different nature and polarity), problems of wetting can arise. Thus, the second difficulty when using the blade-coating technique is the incompatible surface energy of the material film below with the solution formulation under deposition.

Our p-type ink was deposited directly on ITO. The 95:5 = H_2O: BA (v/v) solvent ratio, proposed in the work of Aqoma et al.[56] for the p-type ink, was very efficient to disperse them, but the underlying ITO wettability was severely hampered (see Figure S2). The use of very polar solvents (water) for thin film deposition introduces several difficulties, including the slow evaporation and matching with the substrate's wettability. Thus, we reduced our p-type inks' polarity by using a solvent system containing 50% BA and 50% H_2O. We should also mention that this shift compromises the colloidal stability of the p-type inks to a certain extent. MPA-PbS CQD inks in the mixture of 95:5 = H_2O:BA are stable for around one day, while in the mixture of 5:95 = H_2O:BA, they precipitate within an hour.

From the device viewpoint, our current device geometry without an HTL is not ideal, as it can show lower reproducibility and leaky devices. The introduction of a proper HTL might result in a reduced surface recombination and, consequently, a higher V_{OC} and PCE.

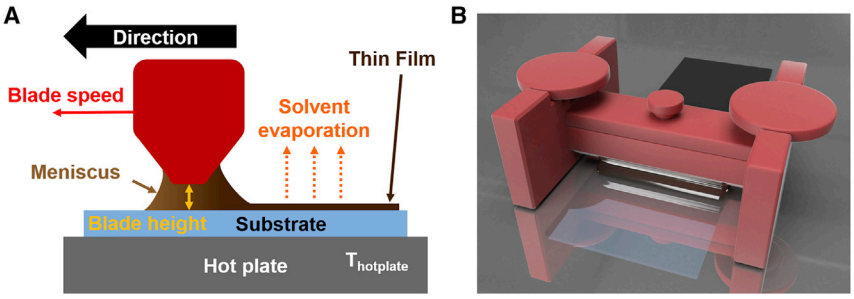

Figure 2. Blade-coating technique
(A) A schematic of a blade-coater device.
(B) A rendering of a blade coater whereby the blade's movement over the substrate deposits a thin film of quantum dots.

While we are convinced that our architecture will benefit the introduction of an HTL, we also have to be realistic about possible options. The HTL utilized in previous studies is not optimal. The NiO_x used in a recent study[41] requires an annealing temperature of 275°C. These conditions are incompatible both with tandem architectures and with plastic substrates.[57,58]

Novel conjugated polymers as PDTPBT (poly[2,6-(N-(1-pentylhexyl)dithieno [3,2-b:20,30-d]pyrrole)-alt-4,7-(2,1,3-benzothiadiazole)]), proposed recently as an HTL for CQD solar cells, are promising but require expensive and elaborate multistep synthesis.[13,56] Thus, the prices of the synthesis of these polymers will undermine the concept of low-cost and scalable devices.

Our attempts to use HTLs, such as Poly[bis(4-phenyl)(2,4,6-trimethylphenyl)amine (PTAA) and Poly(N,N'-bis-4-butylphenyl-N,N'-bisphenyl)benzidine (Poly-TPD), which were recently successfully used for perovskite solar cells, gave rise to lower PCE than in their absence. We believe this is determined by the inability to get a continuous layer of Poly-TPD because of the very polar solvent combination used for the active layer. We suspect that these solvents can partially redissolve the mentioned polymers. Thereby, the selection and optimization of suitable materials as an HTL would require extra efforts.

Solar-cell characterization and evaluation

Figures 3A and 3B show atomic force microscopy (AFM) micrographs of a PbS-MPA layer deposited on ITO and the underlying ITO topography, respectively. The variation in height of the PbS-MPA corresponds to the thickness of the layer, as measured with a profilometer (around 40 nm). Therefore, despite the film exhibiting a generally good morphology and limited overall surface roughness (6.1 nm), there are pinholes that reach through the entire film. These pinholes could result in parasitic shunt paths in devices and affect the reproducibility of performances. Pinholes can also propagate on the n-type layer. However, it is expected that they are partially mitigated by the solution-casting of the ZnO nanoparticles (ETL). The ZnO NC layer in the devices shown in this paper was still deposited by spin coating. We also tried to deposit ZnO NCs in the same device architecture by blade coating (from either $CHCl_3$ solutions or MeOH:$CHCl_3$ = 1:1 solutions), and this resulted in working devices. That is why we are convinced it will be possible in the near future to deposit this layer by blade coating after proper adjustment of the deposition parameters in order to get an optimal and reliable thickness of the ZnO NC layer and good morphology.

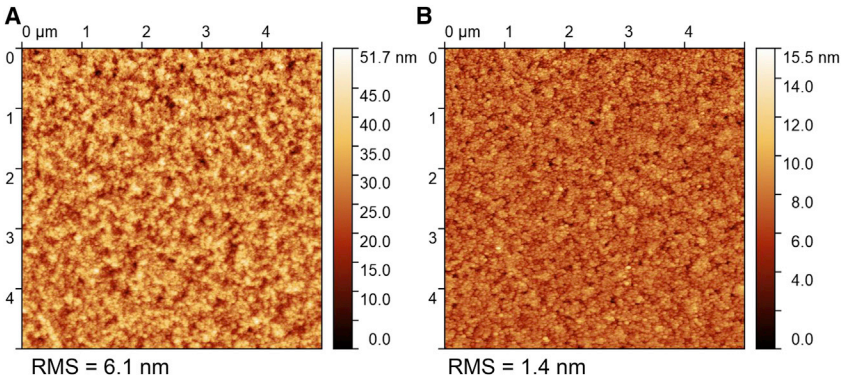

Figure 3. AFM micrographs

(A and B) AFM micrographs showing a 5 × 5 μm^2 scan size of (A) a PbS-MPA layer deposited on ITO showing an RMS (root mean square) of 6.1 nm and (B) underlying ITO showing an RMS of 1.4 nm.

The J-V measurements under illumination and in the dark are shown in the main panel and the inset of Figure 4A, respectively. During operation under standard AM1.5 conditions at 295 K, the J-V-characteristics of the solar cell change significantly, reaching a maximum value after 70 min of illumination. While the variation of the short circuit current density after illumination is minimal, both the V_{OC} (open circuit voltage) and the FF (fill factor) increase significantly. The J_{SC} (short circuit current density) measured from the reverse sweep increases from 24.8 mA cm^{-2} to 26.2 mA cm^{-2} during operation, and the V_{OC} increases from 0.27 V to 0.57 V. Similarly, the FF increases from 0.45 to 0.61. The significant improvement of the device parameters after illumination results in the PCE increasing from 2.96% to 9.04%. Importantly, the hysteresis of the J-V curves also almost disappeared after 70 min of illumination.

It is also interesting to note that the dark current is modified by the illumination, as shown in the inset of Figure 4A. The reverse saturation current density decreases by about two orders of magnitude after illumination.

The external quantum efficiency (EQE) spectrum is shown in Figure 4B; the first excitonic peak appears as a shoulder at 950 nm, corresponding with the absorption spectrum of the CQDs in solution (Figure S1). However, the EQE spectrum does not fully correspond to the absorption spectrum because of the redistribution of the light absorption due to cavity effects, which determines interference effects for certain wavelengths. Integrating the EQE data, a J_{SC} of 21.0 mA cm^{-2} was determined; this is a few mA below what is measured with the J-V characteristics. The integrated J_{SC} is shown in blue on the right axis. It is important to note that the J-V characteristics shown in Figure 4A and the EQE data shown in Figure 4B were measured on different days. The sensitivity of the devices to the duration of illumination and the limited intensity of the bias light during the EQE measurements may be factors explaining the variation of the J_{SC} measured with the two techniques.

The effect of the illumination as a function of time on the figures-of-merit measured from the J-V-characteristics is displayed in Figure 5. The device's stability is also demonstrated, as the same measurement was performed on multiple days after storage of the devices in N_2-atmosphere. All these figures-of-merit—the J_{SC}, V_{OC}, FF, and PCE—increase during the operation of the CQD solar cells, but after the storage in N_2, the rate at which the values stabilized seems to lengthen, and the magnitude

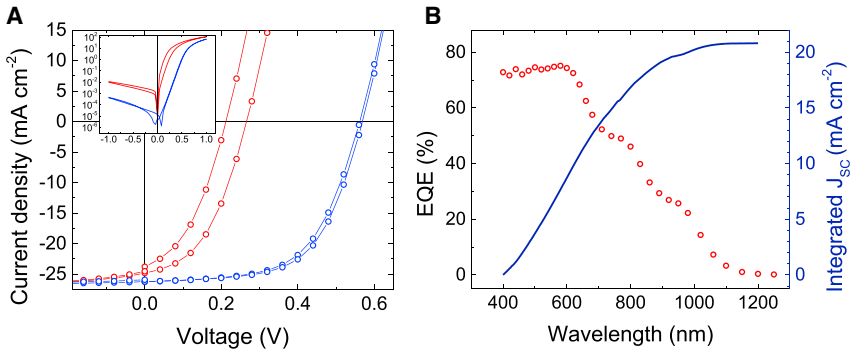

Figure 4. Device performance

(A) The current density versus voltage characteristics of the champion ITO/PbS-MPA/PbS-PbX_2/ZnO/Al device right as the device was exposed to one sun illumination (red) and after 70 min of constant illumination (blue). The inset shows the absolute current density in the dark right before illumination (red) and after 70 min of illumination (blue).

(B) The EQE spectra of the champion device (red) on the left axis with the integrated J_{SC} (blue) on the right axis.

of the values also decreases indicating degradation of the devices. The lengthening can especially be seen in the V_{OC} and FF, while the J_{SC} seems to stabilize relatively fast. The FF does not stabilize to its initial value after storage, which is the main reason the PCE does not increase to the same degree. However, in the time frame of the experiment, the J_{SC} and V_{OC} also did not return to their initial value.

During the operation of the solar cells, the temperature was controlled with a manual liquid-N_2-cooled N_2 stream. Therefore, it was very difficult to ensure the temperature was fully stable for extended periods of time. Some local variations in the plots might be explained by fluctuations in the temperature. Also, the output power of the lamp has been observed to alter slightly.

The J_{SC}, V_{OC}, FF, and PCE of 40 different devices are shown in Table 1, where the champion devices mentioned in Figures 4 and 5 are displayed as the champion devices. Filtering was made whereby devices would only be included if both the V_{OC} and FF were greater than 0.4 V and 0.4, respectively. This limit was chosen such that devices that did not have good contacts or significant shunt paths would not be added. One reason for the large variation in device performance could be that not all devices were illuminated for the same time and were, therefore, not fully stabilized. Furthermore, the devices were produced with various batches of inks; therefore, variations are present due to a possible difference in the ink preparation. Large variations might also be a result of the presence of pinholes in the active layer. A different number of pinholes can substantially modify the shunt resistance of devices.

The reversible light-soaking effects, as observed in Figure 5, are indicative of a photo-activated process, which is also in agreement with the discussed difference between the current measured in the J-V characteristics and the one measured in the EQE. Similar effects have been reported several times not only for CQD-based devices but also for metal halide perovskite solar cells.[59] The effect is often attributed to the interfacial trap filling occurring under illumination, which determines the increased V_{OC}.[59,60] Furthermore, the ZnO layer might also become more doped upon light exposure, increasing the strength of the electric field in the p-n junction.[61,62] We have seen a similar effect of the light soaking in our previous study, where the n-p structure was investigated with TiO_2 as wide band-gap oxide material ETL.[63]

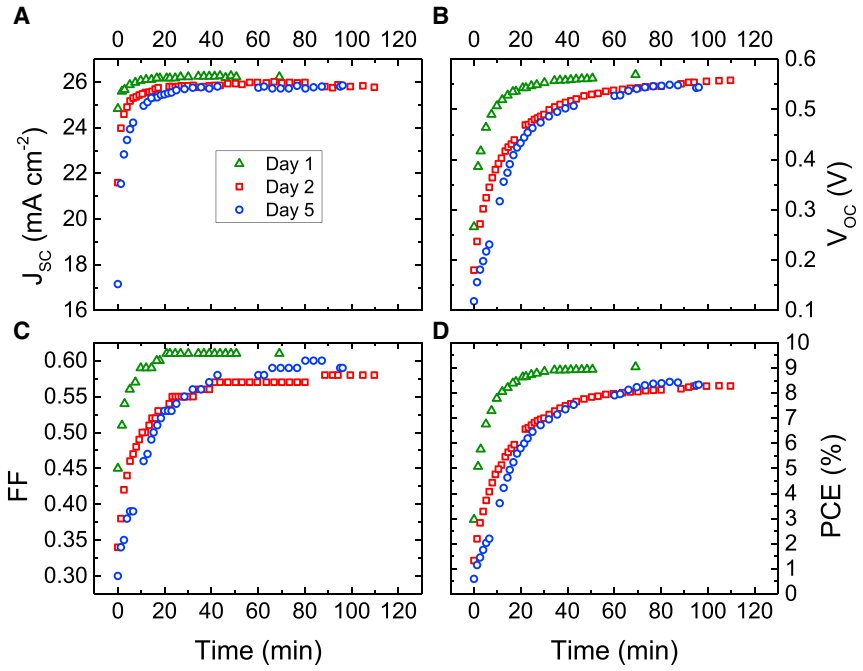

Figure 5. The effect of illumination on the device performance

(A–D) J_{SC} (A), V_{OC} (B), FF (C), and PCE (D) measured on three different days of the champion ITO/PbS-MPA/PbS-PbX_2/ZnO/Al device. The device was stored in an N_2-atmosphere in between the tests. At 0 min, the shutter was removed, and the device was illuminated.

We therefore analyzed devices after light soaking, assuming that the photo-current followed a power law and used light-intensity dependence measurements (shown in Figure S3), which resulted in an $\alpha = 0.94 \pm 0.03$ and an ideality factor $n = 1.35 \pm 0.06$. The α coefficient close to unity indicates that bimolecular recombination is not severe in this case, while the non-unity of the ideality factor suggests some trap-assisted recombination, which is a quite common feature in this type of devices.

As mentioned, the efficiency of the champion device is around 9%, which is very close to the record reported for this geometry using spin-coated-based LbL methods and NiO_x as an HTL (9.7%).[41] Despite using NiO_x as an HTL, these devices showed a lower V_{OC} value (0.53 V versus our 0.57 V), even considering that CQDs with a similar band gap have been used in both studies. Another study with same geometry also using the LbL deposition technique showed an efficiency of 8.45%.[42] In this case, to achieve the best performance, they proposed using an additional HTL on top of ITO (PDTPBT), which actually improved the V_{OC} (0.63 V). However, this device shows a much lower J_{SC} value (20.39 mA cm^{-2} versus our 26.22 mA cm^{-2}), and their reference device, consisting of only a PbS CQD p-n junction and without an additional HTL, has a comparable V_{OC} to our value and considerably lower PCE of 7.17%.

We demonstrated the fabrication of a p-n structure solar cell where the active layer is produced at ambient conditions with a potentially scalable blade-coating technique. The layer casting and the solution-based ligand exchanges were accomplished under ambient conditions, which greatly simplified fabrication and allowed for high throughput. The active layer was obtained by sequential blade casting of PbS CQDs capped by MPA (p-type inks) and lead halides (n-type inks); especially

Table 1. The extracted J-V characteristics

	Sweep direction	J_{SC} (mA cm^{-2})	V_{OC} (V)	FF	PCE (%)
Champion	reverse	26.22	0.57	0.61	9.04
Average (40 devices)	reverse	24.3 ± 2.1	0.54 ± 0.04	0.52 ± 0.06	6.8 ± 1.0
Champion	forward	26.27	0.56	0.59	8.75
Average (40 devices)	forward	24.7 ± 1.9	0.53 ± 0.04	0.50 ± 0.06	6.5 ± 1.0

J_{SC}, V_{OC}, FF and PCE from 40 different ITO/PbS-MPA/PbS-PbX_2/ZnO/Al devices. The parameters are extracted after light soaking stabilization.

important is the optimization of the p-type ink with sufficient colloidal stability, the optimization of the substrate wettability, and the possibility to find orthogonal solvents. As a result, CQD solar cells with p-n architecture fully blade coated accomplished a PCE of 9.0%. This result is very close to the previously reported record in a p-n structure fabricated by spin coating, which is 9.7%, and outperforms it in V_{OC}.[41]

The device exhibits strong light-soaking characteristics, which originate from reversible photo-activated trap filling most probably occurring in the ZnO ETL. Importantly, our device's storage stability is good, since upon keeping the devices in ambient conditions for 2 weeks, the efficiency remains practically unchanged (Figure S4).

EXPERIMENTAL PROCEDURES

Resource availability

Lead contact

Further information and requests should be directed to and will be fulfilled by the lead contact, Maria A. Loi (m.a.loi@rug.nl).

Materials availability

This study did not generate new unique materials.

Data and code availability

The published article includes all of the data analyzed and necessary to reach the conclusions of this study in the figures and tables of the main text and the Supplemental information.

Preparing PbS-OA

PbS CQDs capped with oleate ligands were synthesized by the hot injection method.[64] As a lead precursor, 18 g of lead (II) oxide were used. This powder was mixed with 744 mL octadecene (ODE) and 56 mL OA. Then, the lead precursor solution was dried for 1 h under vacuum (1 mbar) at 140°C in a three-neck reaction flask using a Schlenk line. As a sulfur precursor, bis(trimethylsilyl)sulfide (TMS_2S) was used: 8.4 mL of TMS_2S were dissolved in 400 mL of dried ODE in a closed addition funnel in the nitrogen-filled glovebox. The addition funnel was attached to the flask with lead oleate solution. The reaction was carried out under the nitrogen atmosphere. The lead precursor solution was heated to 110°C, and when the temperature reached this point, heating was turned off, and the flask was evacuated down to 5 mbar. After that, the valve of the addition funnel was opened, and the sulfur precursor solution was quickly injected to the lead precursor solution. Upon complete injection, the flask was recharged with nitrogen. After 8 min of QD growth, the reaction was quenched by cooling the reaction flask down to room temperature using a cold-water bath. Hexane (0.6 L) and ethanol (6 L) were added to the crude solution, followed by centrifugation. CQDs were again re-dispersed in 0.6 L hexane and precipitated by 1.1 L of ethanol. For the third washing cycle, 0.3 L hexane and 0.46 L ethanol

were used. Finally, PbS CQDs were re-dispersed in 100 mL of anhydrous hexane inside the glovebox. Solution concentrations were determined by the measurement of the absorption of diluted solutions at 400 nm.[65]

Preparation of the p-type ink

The p-type ink was formed in solution-phase ligand exchange with a slightly modified recipe with respect to the one reported in the literature.[14] A solution of 3-MPA (Sigma Aldrich, 99%) in N,N-Dimethylformamide (DMF) (38.3 mM) was added (in equal volumes [3 ml]) to a solution of PbS-OA in hexane (8 mg mL^{-1}). The mixture was vigorously shaken manually. After that, the ligand exchange was very rapid (< 10 s), as evidenced by the change of color of the two solvent phases. At this point, the hexane phase containing the OA ligands was removed, and the solution was washed two times with an equal volume of hexane to get rid of the residual aliphatic ligands. After washing, the solution was centrifuged for 5 min at 4,500 RCF. The supernatant was removed, and the remnant pellet was dissolved in a 600 μL mixture of water and BA (H_2O:BA 50:50) to achieve a concentration of around 40 mg mL^{-1}. Before using the solution for device fabrication, it was filtered with a 0.2 μm PTFE filter to remove eventual agglomerates. Here, it is essential to underline that the concentration of MPA used was larger than that mentioned in the article by Aqoma et al.,[56] as the complete ligand exchange could not be achieved using the concentration mentioned in the literature.[14]

Preparation of the n-type ink

The n-type ink was formed using a similar solution-phase ligand exchange method as described above, following the literature reports.[11] Briefly, solutions in DMF of PbI_2 (Sigma Aldrich, 99.999%), $PbBr_2$ (Sigma Aldrich, 99.999%), and ammonium acetate (AA, Sigma Aldrich 99.99%) with concentrations of 0.1 M, 0.02 M, and 0.06 M, respectively, were prepared and were referred to as PbX_2. A volume of 20 mL of the PbX_2 solution was added to about 12.5 mL PbS-OA (10 mg ml^{-1}) in hexane.

The biphasic mixture was shaken vigorously for around 45 s, during which the ligand exchange took place. The less-dense hexane solution was removed, and the polar phase was washed with 10 mL of fresh hexane. This washing step was subsequently repeated two more times. After the third washing step, 10 mL of toluene antisolvent was added, and the solution was then centrifuged at 4,500 RCF for 5 min. The supernatant was removed. The pellet was dried inside a vacuum oven. To create the ink suitable for deposition, 800 μL of BA was added, and the ink was filtered through a 0.2 μm PTFE filter.

Preparing ZnO

The ZnO NCs were made using a slightly altered recipe than the one proposed by Weller et al.[66,67] First, 5.90 g of zinc acetate dehydrate (Alfa Aesar, ACS, 98.0%–101.0%) was stirred with 250 mL of methanol (MeOH) at 60°C. Afterward, 2.96 g of KOH (Sigma Aldrich, 99.99%) was dissolved in 130 mL of MeOH. The KOH solution was added to the zinc acetate dihydrate solution within 10 min during vigorous stirring. The mixture first became cloudy and then again turned transparent quickly afterward. After around 90 min, the solution became turbid. The heating and stirring were stopped after about 2 h. The suspended ZnO NCs were precipitated overnight. Then, the supernatant was removed, and 100 mL of fresh MeOH was added for NC washing. After a short period of vigorous stirring, the ZnO NCs were again allowed to settle down, and the washing step was repeated. Before deposition, the ZnO NCs were dissolved in a mixture of methanol and chloroform (MeOH:$CHCl_3$ = 1:1 v/v) with a concentration of 68 mg/mL.

Device fabrication

Pre-patterned ITO substrates were cleaned by scrubbing them in soapy water. Afterward, the substrates were sonicated twice with MilliQ water for 10 min, followed by sonication in acetone for 15 min and 15 min in isopropyl alcohol. Then, the substrates were dried overnight in an oven at 130°C.

Before the deposition of the p-type layer, the substrates were treated by oxygen plasma for 3 min. The p-type ink is deposited directly on the patterned ITO substrates using a blade coater with stage heated to 70°C at a rate of 7.5 mm/s at ambient conditions. A schematic of a blade coater in action is shown in a Figure 2. The height of the blade was about 200 μm above the substrate. These conditions yielded a layer thickness of around 40 nm measured by profilometry. The PbS-MPA films were annealed at 100°C for at least 10 min. The n-type ink was blade coated on top of the PbS-MPA layer at a blade speed of 80 mm/s with the stage at 50°C, also at ambient conditions. A blade height of about 50 μm was used, and subsequently, the devices were annealed at 70°C for 10 min. The thickness of this layer was measured to be roughly 380 nm.

The device then finished with an ETL and the cathode. A ZnO NC layer was spin-coated at 7,000 rpm for 30 s. Using these parameters and the concentration mentioned prior, a layer of about 50 nm was obtained.

Finally, a 100-nm aluminum electrode was deposited by thermal evaporation through a shadow mask. The chamber pressure during deposition was around 5×10^{-7} mbar.

J-V measurements

The measurements for the current density-voltage characteristics were conducted in N_2-atmosphere at 295 K. A Keithley 2400 source meter was used to change the voltage and measure the current. The temperature was controlled using a cooled N_2 stream. The AM1.5 solar spectrum was simulated using a Steurnagel Solar constant 1200 metal halide lamp, and a silicon calibration cell (WRVS reference cell, Fraunhofer ISE) was used to position the sample to the illumination of 100 mW/cm^2. The area used to determine the dark current is the one where the bottom and top electrodes overlap. Our substrates provide four areas which differ by size (0.09 cm^2, 0.16 cm^2, 0.36 cm^2, 1.01 cm^2). The areas for the measurements under illumination were defined by the shadow masks with the slightly smaller area than the one defined by the electrodes overlap, in order to exclude lateral contributions to the J_{SC} from beyond the device area. Thus, devices active areas were 0.04 cm^2, 0.09 cm^2, 0.25 cm^2, and 0.8 cm^2. For the statistical analysis, we used devices with the active areas of 0.04 cm^2 and 0.09 cm^2. However, devices with larger areas showed comparable efficiencies.

For the light-intensity dependence measurement, neutral density filters were used with optical densities ranging from 0.1 to 1 with 0.1 increments. The devices were first allowed to stabilize under one sun illumination before optical filters were incrementally changed to higher optical densities.

EQE measurements

The EQE was measured using monochromatic light. To create the monochromatic light, a white light 230 W quartz tungsten halogen light (6334NS, Newport) was used together with a set of narrow bandpass filters (Thorlabs). These filters have a full-width half-maximum of 10 $\pm$ 2 nm from 400 to 1300 nm and 12 $\pm$ 2.4 nm from 1,300 to 1,400 nm. The effect of background light was removed using a lock-in

amplifier together with a chopper at 60 Hz. The light intensity was measured using two calibrated photodiodes, a PD300 and PD300IR (Ophir Optics), for the visible and near IR regions, respectively.

Absorbance and PL measurements

UV-VIS-IR absorption spectra were collected using a Jasco V670 spectrometer. Fluorolog iHR 320 Horiba Jobin Yvon spectrofluorimeter equipped with an InGaAs detector was used to acquire steady-state PL spectra. The excitation wavelength was 400 nm, as provided by a 450W Xenon lamp dispersed with a monochromator. Measured intensities were corrected to take into account the spectral response of the InGaAs detector. NCs were dissolved in TCE for absorption and PL spectroscopies.

Morphological characterization

AFM measurements were obtained with a Bruker microscope (MultiMode 8 with ScanAsyst) in ScanAsyst Peak Force Tapping mode with SCANASYST-AIR probes under ambient conditions, having elastic constant k = 0.4 N m^{-1}, a resonance frequency of 70 kHz, and a tip radius less than 12 nm (nominal 2 nm). The images were taken with a scan rate of 0.98 Hz and the resolution of 1,024 lines/sample.

SUPPLEMENTAL INFORMATION

Supplemental information can be found online at https://doi.org/10.1016/j.xcrp.2021.100655.

ACKNOWLEDGMENTS

V.M.G., N.V.S., and M.A.L. acknowledge the financial support of the ERC Starting Grant "Hybrids Solution Processable Optoelectronic Devices" (Hy-SPOD) (ERC306983). Teodor Zaharia and Arjen Kamp are acknowledged for technical support.

AUTHOR CONTRIBUTIONS

V.M.G. and N.V.S. contributed equally to this work. V.M.G. carried out the device fabrication and measurements, and N.V.S. guided and helped the device fabrication and characterization. D.N.D. and M.V.K. synthesized PbS CQDs and carried out the absorbance and PL measurements. M.A.L. supervised this project. All authors contributed to the discussion and interpretation of the results and completion of the manuscript.

DECLARATION OF INTERESTS

M.A.L. is on the advisory board of *Cell Reports Physical Science*. The other authors declare no competing interests.

Received: August 19, 2021
Revised: October 9, 2021
Accepted: October 29, 2021
Published: November 16, 2021

REFERENCES

1. Balazs, D.M., and Loi, M.A. (2018). Lead-Chalcogenide Colloidal-Quantum-Dot Solids: Novel Assembly Methods, Electronic Structure Control, and Application Prospects. Adv. Mater. *30*, 1800082.

2. Brown, P.R., Kim, D., Lunt, R.R., Zhao, N., Bawendi, M.G., Grossman, J.C., and Bulović, V. (2014). Energy level modification in lead sulfide quantum dot thin films through ligand exchange. ACS Nano *8*, 5863–5872.

3. Voznyy, O., Zhitomirsky, D., Stadler, P., Ning, Z., Hoogland, S., and Sargent, E.H. (2012). A charge-orbital balance picture of doping in colloidal quantum dot solids. ACS Nano *6*, 8448–8455.

4. Shulga, A.G., Yamamura, A., Tsuzuku, K., Dragoman, R.M., Dirin, D.N., Watanabe, S., Kovalenko, M.V., Takeya, J., and Loi, M.A. (2019). Patterned Quantum Dot Photosensitive FETs for Medium Frequency

Optoelectronics. Adv. Mater. Technol. *4*, 1900054.

5. Bederak, D., Balazs, D.M., Sukharevska, N.V., Shulga, A.G., Abdu-Aguye, M., Dirin, D.N., Kovalenko, M.V., and Loi, M.A. (2018). Comparing Halide Ligands in PbS Colloidal Quantum Dots for Field-Effect Transistors and Solar Cells. ACS Appl. Nano Mater. *1*, 6882–6889.

6. Pradhan, S., Di Stasio, F., Bi, Y., Gupta, S., Christodoulou, S., Stavrinadis, A., and Konstantatos, G. (2019). High-efficiency colloidal quantum dot infrared light-emitting diodes via engineering at the supra-nanocrystalline level. Nat. Nanotechnol. *14*, 72–79.

7. Shulga, A.G., Kahmann, S., Dirin, D.N., Graf, A., Zaumseil, J., Kovalenko, M.V., and Loi, M.A. (2018). Electroluminescence Generation in PbS Quantum Dot Light-Emitting Field-Effect Transistors with Solid-State Gating. ACS Nano *12*, 12805–12813.

8. Kahmann, S., Shulga, A., and Loi, M.A. (2020). Quantum Dot Light-Emitting Transistors—Powerful Research Tools and Their Future Applications. Adv. Funct. Mater. *30*, 1904174.

9. Sliz, R., Lejay, M., Fan, J.Z., Choi, M.-J., Kinge, S., Hoogland, S., Fabritius, T., García de Arquer, F.P., and Sargent, E.H. (2019). Stable Colloidal Quantum Dot Inks Enable Inkjet-Printed High-Sensitivity Infrared Photodetectors. ACS Nano *13*, 11988–11995.

10. Shulga, A.G., Derenskyi, V., Salazar-Rios, J.M., Dirin, D.N., Fritsch, M., Kovalenko, M.V., Scherf, U., and Loi, M.A. (2017). An All-Solution-Based Hybrid CMOS-Like Quantum Dot/Carbon Nanotube Inverter. Adv. Mater. *29*, 1701764.

11. Liu, M., Voznyy, O., Sabatini, R., García de Arquer, F.P., Munir, R., Balawi, A.H., Lan, X., Fan, F., Walters, G., Kirmani, A.R., et al. (2017). Hybrid organic-inorganic inks flatten the energy landscape in colloidal quantum dot solids. Nat. Mater. *16*, 258–263.

12. Xu, J., Voznyy, O., Liu, M., Kirmani, A.R., Walters, G., Munir, R., Abdelsamie, M., Proppe, A.H., Sarkar, A., García de Arquer, F.P., et al. (2018). 2D matrix engineering for homogeneous quantum dot coupling in photovoltaic solids. Nat. Nanotechnol. *13*, 456–462.

13. Kim, H.I., Baek, S.W., Cheon, H.J., Ryu, S.U., Lee, S., Choi, M.J., Choi, K., Biondi, M., Hoogland, S., de Arquer, F.P.G., et al. (2020). A Tuned Alternating D-A Copolymer Hole-Transport Layer Enables Colloidal Quantum Dot Solar Cells with Superior Fill Factor and Efficiency. Adv. Mater. *32*, e2004985.

14. Aqoma, H., and Jang, S.-Y. (2018). Solid-state-ligand-exchange free quantum dot ink-based solar cells with an efficiency of 10.9%. Energy Environ. Sci. *11*, 1603–1609.

15. Kirmani, A.R., Luther, J.M., Abolhasani, M., and Amassian, A. (2020). Colloidal Quantum Dot Photovoltaics: Current Progress and Path to Gigawatt Scale Enabled by Smart Manufacturing. ACS Energy Lett. *5*, 3069–3100.

16. Semonin, O.E., Luther, J.M., and Beard, M.C. (2012). Quantum dots for next-generation photovoltaics. Mater. Today *15*, 508–515.

17. Kim, T., Lim, S., Yun, S., Jeong, S., Park, T., and Choi, J. (2020). Design Strategy of Quantum Dot Thin-Film Solar Cells. Small *16*, e2002460.

18. Weidman, M.C., Beck, M.E., Hoffman, R.S., Prins, F., and Tisdale, W.A. (2014). Monodisperse, air-stable PbS nanocrystals via precursor stoichiometry control. ACS Nano *8*, 6363–6371.

19. Fan, J.Z., Vafaie, M., Bertens, K., Sytnyk, M., Pina, J.M., Sagar, L.K., Ouellette, O., Proppe, A.H., Rasouli, A.S., Gao, Y., et al. (2020). Micron Thick Colloidal Quantum Dot Solids. Nano Lett. *20*, 5284–5291.

20. Fan, J.Z., Andersen, N.T., Biondi, M., Todorović, P., Sun, B., Ouellette, O., Abed, J., Sagar, L.K., Choi, M.J., Hoogland, S., et al. (2019). Mixed Lead Halide Passivation of Quantum Dots. Adv. Mater. *31*, e1904304.

21. Lee, S., Choi, M.-J., Sharma, G., Biondi, M., Chen, B., Baek, S.-W., Najarian, A.M., Vafaie, M., Wicks, J., Sagar, L.K., et al. (2020). Orthogonal colloidal quantum dot inks enable efficient multilayer optoelectronic devices. Nat. Commun. *11*, 4814.

22. Wang, X., Koleilat, G.I., Tang, J., Liu, H., Kramer, I.J., Debnath, R., Brzozowski, L., Barkhouse, D.A.R., Levina, L., Hoogland, S., et al. (2011). Tandem colloidal quantum dot solar cells employing a graded recombination layer. Nat. Photonics *5*, 480–484.

23. Shi, G., Wang, Y., Liu, Z., Han, L., Liu, J., Wang, Y., Lu, K., Chen, S., Ling, X., Li, Y., et al. (2017). Stable and Highly Efficient PbS Quantum Dot Tandem Solar Cells Employing a Rationally Designed Recombination Layer. Adv. Energy Mater. *7*, 1602667.

24. Kim, H.I., Baek, S.W., Choi, M.J., Chen, B., Ouellette, O., Choi, K., Scheffel, B., Choi, H., Biondi, M., Hoogland, S., et al. (2020). Monolithic Organic/Colloidal Quantum Dot Hybrid Tandem Solar Cells via Buffer Engineering. Adv. Mater. *32*, e2004657.

25. Kim, H.I., Lee, J., Choi, M., Ryu, S.U., Choi, K., Lee, S., Hoogland, S., Arquer, F.P.G., Sargent, E.H., and Park, T. (2020). Efficient and Stable Colloidal Quantum Dot Solar Cells with a Green-Solvent Hole-Transport Layer. Adv. Energy Mater. *10*, 2002084.

26. Sun, B., Johnston, A., Xu, C., Wei, M., Huang, Z., Jiang, Z., Zhou, H., Gao, Y., Dong, Y., Ouellette, O., et al. (2020). Monolayer Perovskite Bridges Enable Strong Quantum Dot Coupling for Efficient Solar Cells. Joule *4*, 1542–1556.

27. Choi, M.-J., García de Arquer, F.P., Proppe, A.H., Seifitokaldani, A., Choi, J., Kim, J., Baek, S.-W., Liu, M., Sun, B., Biondi, M., et al. (2020). Cascade surface modification of colloidal quantum dot inks enables efficient bulk homojunction photovoltaics. Nat. Commun. *11*, 103.

28. Wang, Y., Liu, Z., Huo, N., Li, F., Gu, M., Ling, X., Zhang, Y., Lu, K., Han, L., Fang, H., et al. (2019). Room-temperature direct synthesis of semi-conductive PbS nanocrystal inks for optoelectronic applications. Nat. Commun. *10*, 5136.

29. Wang, Y., Lu, K., Han, L., Liu, Z., Shi, G., Fang, H., Chen, S., Wu, T., Yang, F., Gu, M., et al. (2018). In Situ Passivation for Efficient PbS Quantum Dot Solar Cells by Precursor Engineering. Adv. Mater. *30*, e1704871.

30. Bederak, D., Dirin, D.N., Sukharevska, N., Momand, J., Kovalenko, M.V., and Loi, M.A. (2021). S-Rich PbS Quantum Dots: A Promising p-Type Material for Optoelectronic Devices. Chem. Mater. *33*, 320–326.

31. Gu, M., Wang, Y., Yang, F., Lu, K., Xue, Y., Wu, T., Fang, H., Zhou, S., Zhang, Y., Ling, X., et al. (2019). Stable PbS quantum dot ink for efficient solar cells by solution-phase ligand engineering. J. Mater. Chem. A Mater. Energy Sustain. *7*, 15951–15959.

32. Lin, Q., Yun, H.J., Liu, W., Song, H.-J., Makarov, N.S., Isaienko, O., Nakotte, T., Chen, G., Luo, H., Klimov, V.I., and Pietryga, J.M. (2017). Phase-Transfer Ligand Exchange of Lead Chalcogenide Quantum Dots for Direct Deposition of Thick, Highly Conductive Films. J. Am. Chem. Soc. *139*, 6644–6653.

33. Sukharevska, N., Bederak, D., Goossens, V.M., Momand, J., Duim, H., Dirin, D.N., Kovalenko, M.V., Kooi, B.J., and Loi, M.A. (2021). Scalable PbS Quantum Dot Solar Cell Production by Blade Coating from Stable Inks. ACS Appl. Mater. Interfaces *13*, 5195–5207.

34. Choi, H., Lee, J.-G., Mai, X.D., Beard, M.C., Yoon, S.S., and Jeong, S. (2017). Supersonically Spray-Coated Colloidal Quantum Dot Ink Solar Cells. Sci. Rep. *7*, 622.

35. Choi, M.J., Kim, Y., Lim, H., Alarousu, E., Adhikari, A., Shaheen, B.S., Kim, Y.H., Mohammed, O.F., Sargent, E.H., Kim, J.Y., and Jung, Y.S. (2019). Tuning Solute-Redistribution Dynamics for Scalable Fabrication of Colloidal Quantum-Dot Optoelectronics. Adv. Mater. *31*, e1805886.

36. Kirmani, A.R., Sheikh, A.D., Niazi, M.R., Haque, M.A., Liu, M., de Arquer, F.P.G., Xu, J., Sun, B., Voznyy, O., Gasparini, N., et al. (2018). Overcoming the Ambient Manufacturability-Scalability-Performance Bottleneck in Colloidal Quantum Dot Photovoltaics. Adv. Mater. *30*, e1801661.

37. Salazar-Rios, J.M., Sukharevska, N., Speirs, M.J., Jung, S., Dirin, D., Dragoman, R.M., Allard, S., Kovalenko, M.V., Scherf, U., and Loi, M.A. (2018). Enhancing Quantum Dot Solar Cells Stability with a Semiconducting Single-Walled Carbon Nanotubes Interlayer Below the Top Anode. Adv. Mater. Interfaces *5*, 1801155.

38. Chuang, C.-H.M., Brown, P.R., Bulović, V., and Bawendi, M.G. (2014). Improved performance and stability in quantum dot solar cells through band alignment engineering. Nat. Mater. *13*, 796–801.

39. Ning, Z., Voznyy, O., Pan, J., Hoogland, S., Adinolfi, V., Xu, J., Li, M., Kirmani, A.R., Sun, J.P., Minor, J., et al. (2014). Air-stable n-type colloidal quantum dot solids. Nat. Mater. *13*, 822–828.

40. Lai, L.-H., Speirs, M.J., Chang, F.-K., Piveteau, L., Kovalenko, M.V., Chen, J.-S., Wu, J.-J., and Loi, M.A. (2015). Increasing photon absorption and stability of PbS quantum dot solar cells using a ZnO interlayer. Appl. Phys. Lett. *107*, 183901.

41. Wang, R., Wu, X., Xu, K., Zhou, W., Shang, Y., Tang, H., Chen, H., and Ning, Z. (2018). Highly

Efficient Inverted Structural Quantum Dot Solar Cells. Adv. Mater. *30*, 1704882.

42. Lu, K., Wang, Y., Yuan, J., Cui, Z., Shi, G., Shi, S., Han, L., Chen, S., Zhang, Y., Ling, X., et al. (2017). Efficient PbS quantum dot solar cells employing a conventional structure. J. Mater. Chem. A Mater. Energy Sustain. *5*, 23960–23966.

43. Meng, L., Xu, Q., Thakur, U.K., Gong, L., Zeng, H., Shankar, K., and Wang, X. (2020). Unusual Surface Ligand Doping-Induced p-Type Quantum Dot Solids and Their Application in Solar Cells. ACS Appl. Mater. Interfaces *12*, 53942–53949.

44. Ko, D.-K., Maurano, A., Suh, S.K., Kim, D., Hwang, G.W., Grossman, J.C., Bulović, V., and Bawendi, M.G. (2016). Photovoltaic Performance of PbS Quantum Dots Treated with Metal Salts. ACS Nano *10*, 3382–3388.

45. Peng, J., Chen, Y., Zhang, X., Dong, A., and Liang, Z. (2016). Solid-State Ligand-Exchange Fabrication of $CH_3NH_3PbI_3$ Capped PbS Quantum Dot Solar Cells. Adv. Sci. (Weinh.) *3*, 1500432.

46. Speirs, M.J., Dirin, D.N., Abdu-Aguye, M., Balazs, D.M., Kovalenko, M.V., and Loi, M.A. (2016). Temperature dependent behaviour of lead sulfide quantum dot solar cells and films. Energy Environ. Sci. *9*, 2916–2924.

47. Bederak, D., Sukharevska, N., Kahmann, S., Abdu-Aguye, M., Duim, H., Dirin, D.N., Kovalenko, M.V., Portale, G., and Loi, M.A. (2020). On the Colloidal Stability of PbS Quantum Dots Capped with Methylammonium Lead Iodide Ligands. ACS Appl. Mater. Interfaces *12*, 52959–52966.

48. Cao, Y., Stavrinadis, A., Lasanta, T., So, D., and Konstantatos, G. (2016). The role of surface passivation for efficient and photostable PbS quantum dot solar cells. Nat. Energy *1*, 16035.

49. Xu, F., Gerlein, L.F., Ma, X., Haughn, C.R., Doty, M.F., and Cloutier, S.G. (2015). Impact of Different Surface Ligands on the Optical Properties of PbS Quantum Dot Solids. Materials (Basel) *8*, 1858–1870.

50. Yang, Z., Fan, J.Z., Proppe, A.H., Arquer, F.P.G., Rossouw, D., Voznyy, O., Lan, X., Liu, M., Walters, G., Quintero-Bermudez, R., et al. (2017). Mixed-quantum-dot solar cells. Nat. Commun. *8*, 1325.

51. Kovalenko, M.V., Bodnarchuk, M.I., Zaumseil, J., Lee, J.-S., and Talapin, D.V. (2010). Expanding the chemical versatility of colloidal nanocrystals capped with molecular metal chalcogenide ligands. J. Am. Chem. Soc. *132*, 10085–10092.

52. Beygi, H., Sajjadi, S.A., Babakhani, A., Young, J.F., and van Veggel, F.C.J.M. (2018). Solution phase surface functionalization of PbS nanoparticles with organic ligands for single-step deposition of p-type layer of quantum dot solar cells. Appl. Surf. Sci. *459*, 562–571.

53. Balazs, D.M., Bijlsma, K.I., Fang, H.-H., Dirin, D.N., Döbeli, M., Kovalenko, M.V., and Loi, M.A. (2017). Stoichiometric control of the density of states in PbS colloidal quantum dot solids. Sci. Adv. *3*, eaao1558.

54. Kirmani, A.R., Walters, G., Kim, T., Sargent, E.H., and Amassian, A. (2020). Optimizing Solid-State Ligand Exchange for Colloidal Quantum Dot Optoelectronics: How Much Is Enough? ACS Appl. Energy Mater. *3*, 5385–5392.

55. Bisri, S.Z., Piliego, C., Yarema, M., Heiss, W., and Loi, M.A. (2013). Low driving voltage and high mobility ambipolar field-effect transistors with PbS colloidal nanocrystals. Adv. Mater. *25*, 4309–4314.

56. Aqoma, H., Al Mubarok, M., Lee, W., Hadmojo, W.T., Park, C., Ahn, T.K., Ryu, D.Y., and Jang, S.-Y. (2018). Improved Processability and Efficiency of Colloidal Quantum Dot Solar Cells Based on Organic Hole Transport Layers. Adv. Energy Mater. *8*, 1800572.

57. Zhang, X., Öberg, V.A., Du, J., Liu, J., and Johansson, E.M.J. (2018). Extremely lightweight and ultra-flexible infrared light-converting quantum dot solar cells with high power-per-weight output using a solution-processed bending durable silver nanowire-based electrode. Energy Environ. Sci. *11*, 354–364.

58. Zhang, X., Santra, P.K., Tian, L., Johansson, M.B., Rensmo, H., and Johansson, E.M.J. (2017). Highly Efficient Flexible Quantum Dot Solar Cells with Improved Electron Extraction Using MgZnO Nanocrystals. ACS Nano *11*, 8478–8487.

59. Shao, S., Abdu-Aguye, M., Qiu, L., Lai, L.-H., Liu, J., Adjokatse, S., Jahani, F., Kamminga, M.E., ten Brink, G.H., Palstra, T.T.M., et al. (2016). Elimination of the light soaking effect and performance enhancement in perovskite solar cells using a fullerene derivative. Energy Environ. Sci. *9*, 2444–2452.

60. Choi, M.J., Oh, J., Yoo, J.K., Choi, J., Sim, D.M., and Jung, Y.S. (2014). Tailoring of the PbS/metal interface in colloidal quantum dot solar cells for improvements of performance and air stability. Energy Environ. Sci. *7*, 3052–3060.

61. Choi, J.J., Wenger, W.N., Hoffman, R.S., Lim, Y.F., Luria, J., Jasieniak, J., Marohn, J.A., and Hanrath, T. (2011). Solution-processed nanocrystal quantum dot tandem solar cells. Adv. Mater. *23*, 3144–3148.

62. Bhandari, K.P., Roland, P.J., Gao, J., and Ellingson, R.J. (2013). Bandgap, window layer thickness, and light soaking effects on PbS quantum dot solar cells. 2013 IEEE 39th Photovoltaic Specialists Conference (PVSC) (Institute of Electrical and Electronics Engineers Inc.), pp. 258–263.

63. Sukharevska, N., Bederak, D., Dirin, D., Kovalenko, M., and Loi, M.A. (2020). Improved Reproducibility of PbS Colloidal Quantum Dots Solar Cells Using Atomic Layer-Deposited TiO_2. Energy Technol. (Weinheim) *8*, 1900887.

64. Yarema, M., Yarema, O., Lin, W.M.M., Volk, S., Yazdani, N., Bozyigit, D., and Wood, V. (2017). Upscaling Colloidal Nanocrystal Hot-Injection Syntheses via Reactor Underpressure. Chem. Mater. *29*, 796–803.

65. Moreels, I., Lambert, K., Smeets, D., De Muynck, D., Nollet, T., Martins, J.C., Vanhaecke, F., Vantomme, A., Delerue, C., Allan, G., and Hens, Z. (2009). Size-dependent optical properties of colloidal PbS quantum dots. ACS Nano *3*, 3023–3030.

66. Pacholski, C., Kornowski, A., and Weller, H. (2002). Self-assembly of ZnO: from nanodots to nanorods. Angew. Chem. Int. Ed. Engl. *41*, 1188–1191.

67. Beek, W.J.E., Wienk, M.M., Kemerink, M., Yang, X., and Janssen, R.A.J. (2005). Hybrid zinc oxide conjugated polymer bulk heterojunction solar cells. J. Phys. Chem. B *109*, 9505–9516.